








Simulation Analysis of Inverting Marine Vertical Deflection Using Spaceborne GNSS-R Interferometric Altimetry

Lichang Duan , Junming Xia , Weihua Bai , Zhenhe Zhai, Feixiong Huang , *Member, IEEE*, Cong Yin , Yueqiang Sun, Qifei Du, Dongwei Wang, Xianyi Wang , Yixuan Sun, Shengyu Kang, Guanyi Wang, Xiaofeng Meng, and Yunlong Du 

Abstract—Global marine vertical deflection is essential for understanding Earth’s internal mass and density distribution and improving the long-term inertial navigation accuracy of underwater vehicles. Spaceborne global navigation satellite system reflectometry (GNSS-R) interferometric altimetry, with its advantages of low-cost, rapid global coverage, and revisiting capability, shows promise as new data for compensating the radar altimeters. In this study, we present the first simulation of spaceborne GNSS-R interferometric altimetry data based on FY-3E GNSS-R trajectory and evaluate its potential for inverting global marine vertical deflection. Our results showed that, in the operational scenario (with a spatial resolution of 10 km and an altimetry accuracy of 14.68 cm), the total accuracy of marine vertical deflection for global 2.5', 5', and 20' grids, obtained from ten years of simulation data, was 4.998", 1.268", and 0.1", respectively. Furthermore, we observed that, when the average global revisit times reached approximately 90 times and 6 times, the total accuracy of marine vertical deflection for global 5' and 20' grids was below 1". As the GNSS-R detection on the FY-3E satellite covers 90% of the global sea area in 20' grids within 23 days, with an average revisit time of 7.3, spaceborne GNSS-R interferometric altimetry has the potential to invert the high-precision time-variable gravity field with a 20' resolution, thus compensating for the lower resolution provided by satellite gravimetry.

Index Terms—Global navigation satellite system reflectometry (GNSS-R), interferometric altimetry, marine vertical deflection, revisits, satellite altimetry.

I. INTRODUCTION

THE Earth’s gravity field and its spatiotemporal variations provide valuable information about the distribution of internal mass, density, energy transfer, and mass migration within our planet. It is a frontier research area in Earth sciences and is crucial for disciplines, such as geophysics, space science, oceanography, climatology, meteorology, and geodynamics [1]. Vertical deflection, the angle between the actual and normal directions of gravity at a point on the Earth’s surface, is a key parameter used to describe the gravity field, along with gravity anomalies, gravity gradients, and the geoid [2]. Understanding and studying the gravity field is essential for comprehending Earth’s systems and processes [3], [4].

Traditional methods for measuring the gravity field, such as using digital zenith cameras to measure vertical deflection [5] or gravimeters to obtain absolute or relative gravity data [6], are limited in their ability to conduct large-scale measurements. Satellite gravimetry missions, such as the GRACE/GOCE, have significantly advanced the field by providing high-precision gravity data on a global scale every month [7]. However, it primarily captures medium- to long-wavelength information of the gravity field (~ 300 km) and is less sensitive to short-wavelength signals [8]. On the other hand, satellite altimetry, which measures sea surface height (SSH), contains valuable high-frequency information about the Earth’s gravity field. With the development of radar altimetry in recent years, the inversion of marine vertical deflection [9], [10], [11] and gravity anomaly [12], [13], [14] derived from satellite radar altimetry has significantly improved the accuracy and spatial resolution of marine gravity field inversion. While satellite altimetry technology has shown promise, challenges remain in the limited capacity to accommodate radar altimeter antennas on small satellites and the high costs associated with large-scale constellations [15].

Global navigation satellite system reflectometry (GNSS-R) altimetry technology has emerged as a promising and practical complementary solution to overcome these challenges of radar altimetry [16]. GNSS-R is a passive remote sensing technique

Received 4 June 2024; revised 4 November 2024; accepted 16 December 2024. Date of publication 18 December 2024; date of current version 3 January 2025. This work was supported in part by the Youth Innovation Promotion Association, CAS, under Grant 2020152, in part by the National Natural Science Foundation of China under Grant 42104032 and Grant 42074042, in part by the Youth Cross Team Scientific Research Project of the Chinese Academy of Sciences under Grant JCTD-2021-10, and in part by FengYun Application Pioneering Project under Grant FY-APP-2022.0108. (*Corresponding authors: Junming Xia; Weihua Bai.*)

Lichang Duan, Junming Xia, Weihua Bai, Feixiong Huang, Cong Yin, Yueqiang Sun, Qifei Du, Dongwei Wang, Xianyi Wang, Yixuan Sun, Guanyi Wang, Xiaofeng Meng, and Yunlong Du are with the Beijing Key Laboratory of Space Environment Exploration, National Space Science Center, Chinese Academy of Sciences, Beijing 100190, China, and with the Key Laboratory of Science and Technology on Space Environment Situational Awareness, National Space Science Center, Chinese Academy of Sciences, Beijing 100190, China, and also with the University of Chinese Academy of Sciences, Beijing 100049, China (e-mail: duanlichang20@mails.uac.ac.cn; xiajunming@nssc.ac.cn; baiweihua@nssc.ac.cn).

Zhenhe Zhai is with the State Key Laboratory of Geo-Information Engineering, Xi’an 710054, China, and also with the Xi’an Research Institute of Surveying and Mapping, Xi’an 710054, China.

Shengyu Kang is with the School of Computer and Communication Engineering, University of Science and Technology, Beijing 100083, China.

Digital Object Identifier 10.1109/JSTARS.2024.3520186

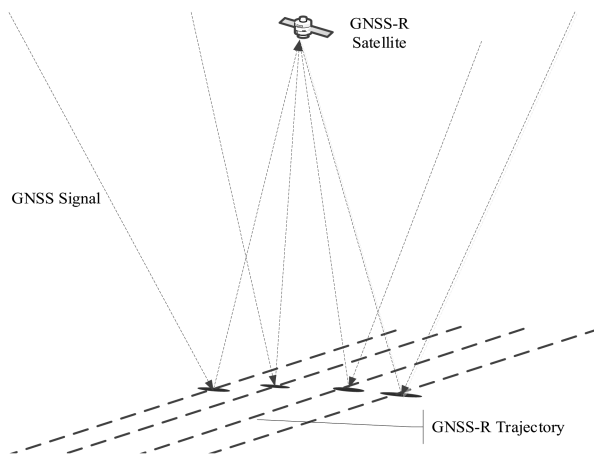


Fig. 1. Diagram of multitrajectory observations for spaceborne GNSS-R.

that utilizes reflected signals from GNSS satellites. It offers advantages, such as all-weather and all-time availability, low power consumption, low cost, easy network implementation, and rapid global coverage [17]. This technology has been successfully applied to various fields, including ocean surface wind speed [18], sea ice [19], [20], and soil moisture [21]. Martin-Neira [22] conducted the first land-based experiment to validate the feasibility of GNSS-R for altimetry. In recent years, various methods for SSH measurements using GNSS-R have been developed, including code altimetry, phase altimetry, dual-antenna interferometry altimetry, and single-antenna signal-to-noise ratio altimetry [23], [24], [25], [26]. Both land-based [27] and airborne [28] experiments have demonstrated GNSS-R altimetry's capability to achieve centimeter-level accuracy. As for the spaceborne GNSS-R, satellite missions include U.K.-Disaster Monitoring Constellation [29], TechDemosat-1 [30], cyclone global navigation satellite system [31], BuFeng-1 A/B, FengYun-3E (FY-3E)/F/G [32], etc. Although these satellite missions have significantly promoted the application of GNSS-R technology, their primary objectives were not focused on SSH measurements due to the suboptimal altimetry precision [33], [34].

To address the precise SSH measurement challenges in spaceborne GNSS-R applications, the PARIS in-orbit demonstrator (IOD) and operational satellite missions were proposed in 2011 [35]. These missions utilize GNSS-R interferometric processing techniques and primarily focus on ocean circulation detection. By performing incoherent integration of power waveforms from multiple samples, spaceborne GNSS-R can achieve decimeter-level SSH measurements with a 100-km along-track spatial resolution. Compared with radar altimetry, GNSS-R interferometric altimetry has a poorer accuracy and a coarser spatial resolution. However, as shown in Fig. 1, spaceborne GNSS-R can simultaneously receive multiple reflections, increasing the number of SSH observations and revisit times, thereby improving global altimetry performance [36]. This technology provides a valuable complement to satellite altimetry products [37] and demonstrates its potential in ocean circulation applications [38]. Furthermore, researchers are optimistic about the application prospects of using GNSS-R altimetry products to invert the

global marine gravity field, considering it a crucial data source for global marine gravity field inversion [39], [40].

However, there has been a lack of research exploring the application of spaceborne GNSS-R interferometric altimetry for gravity field detection using either simulation or practical data. Compared with ocean circulation detection, the detection of the geoid and gravity field places higher demands on altimetry accuracy and spatial resolution. The practical usage and application value of this technology in global marine vertical deflection and gravity field inversion are still uncertain due to limitations in altimetry accuracy, spatial resolution, and the unique characteristics of its reflection trajectories. This study aims to address this gap by evaluating the potential and application value of GNSS-R interferometric altimetry in marine gravity field inversion based on the typical performance of spaceborne GNSS-R interferometric altimetry through simulation.

The rest of this article is organized as follows. Section II analyzes the altimetry accuracy of GNSS-R interferometry and the coverage and revisit capabilities of GNSS-R trajectory data while also providing an overview of the experimental design, data simulation process, and inversion algorithm for marine vertical deflection. In Section III, we present the inversion results and evaluate their accuracy while also analyzing the impact of revisit times on the precision of vertical deflection. Finally, Section IV concludes this article.

II. SIMULATION AND METHODOLOGY DESCRIPTION

A. Spaceborne GNSS-R Specular Points Trajectory

The trajectory of specular points observed by spaceborne GNSS-R is determined by the positions of GNSS satellites, GNSS-R receivers, and the reflection surface, making this pattern unique. This study utilizes GNSS-R trajectories detected by the GNOS-II payload on the FY-3E satellite between July 2021 and September 2023. Launched on 5 July 2021, the FY-3E satellite orbits at an altitude of 836 km with an inclination angle of 98.75° . Equipped with the GNOS-II payload featuring eight signal reception channels, it can simultaneously receive eight specular point trajectories from GPS, BDS, and GALILEO navigation satellite systems. The GNOS-II payload has been working operationally in orbit for over two years [40].

Fig. 2 depicts the trajectory of specular reflection points from the FY-3E satellite within a 24-h period, with different colors indicating different signal reception channels. The Level 2 (L2) data from the FY-3E satellite undergoes strict data control and filtering, resulting in an average utilization of 3.2 channels, rather than fully occupying all eight channels. In addition, with a sampling frequency of 1 Hz, FY-3E L2 GNSS-R trajectory data have a ground spacing distance of 5.6 km between adjacent specular points along the track. In order to ensure that the errors between the adjacent quantities in the simulation results are uncorrelated, we have conducted sparse sampling based on the actual trajectory of FY-3E specular points, resulting in a 10-km spacing between trajectory points. Furthermore, we only selected specular points with an incident angle of less than 35° , in accordance with the parameters used for accuracy analysis in [35].

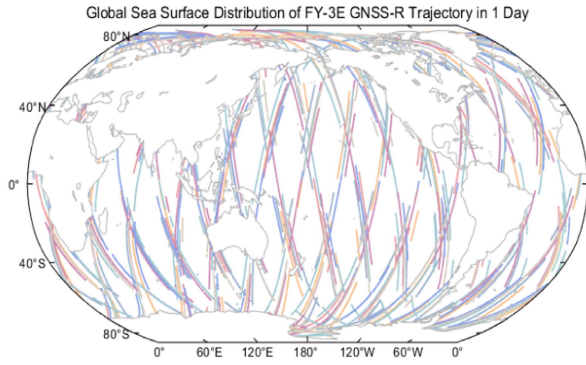


Fig. 2. Global sea surface distribution of FY-3E GNSS-R trajectory in one day, with different colors indicating the trajectories from different signal reception channels.

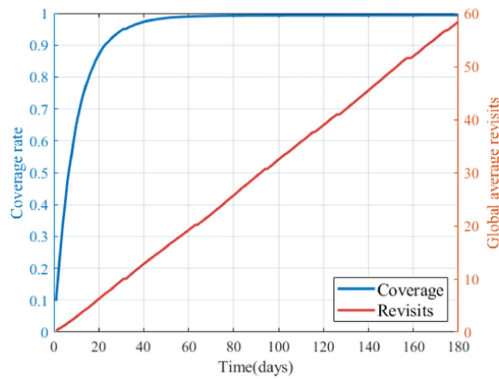


Fig. 3. Temporal evolution of global GNSS-R trajectory coverage and revisit times for marine regions within $\pm 80^\circ$ latitude.

The multichannel observation and large data volume of spaceborne GNSS-R provide a significant advantage in achieving global rapid coverage and multiple revisits. Using the actual trajectory of specular reflection points from FY-3E as an example, Fig. 3 analyzes the coverage rate and revisit times of the global marine region within a latitude range of $\pm 80^\circ$. With the FY-3E L2 data, it is found that 90% coverage of global marine areas at a $20'$ grid can be achieved in 23 days, with an average revisit frequency of 7.3 times. Furthermore, in 62 days, 99% coverage of global marine areas can be achieved, with an average revisit frequency of 19.85 times.

Furthermore, the FY-3E satellite has a designed lifespan of 8 years, allowing for an increase in the coverage range and revisit frequency of GNSS-R specular reflection points as the satellite gains more time in orbit. To further explore the potential of GNSS-R interferometric height inversion for vertical deviations in marine regions, this study conducted simulations of the FY-3E satellite's specular reflection point trajectory for the upcoming years (October 2023–December 2030). This expansion ensures the accurate inversion of high-resolution grid vertical deviations. Fig. 4 illustrates the distribution of revisit times for the global $20'$ grid, using a ten-year dataset of GNSS-R specular point trajectories, including the actual FY-3E satellite trajectory (July 2021–September 2023) and a simulated trajectory (October 2023–December 2030), with an average global revisit frequency of 1054.4 times.

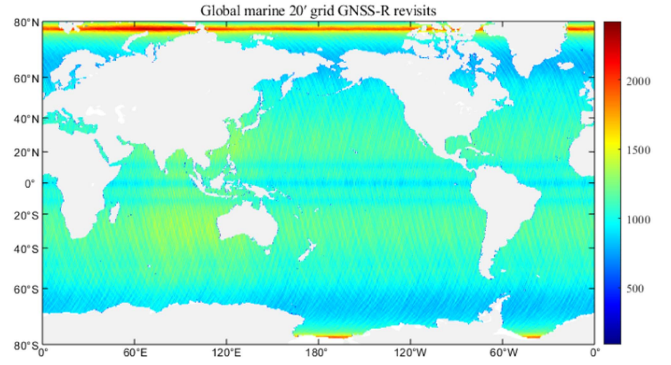


Fig. 4. Distribution of revisit times for the combined actual and simulated GNSS-R trajectories from July 2021 to December 2030 in the global $20'$ grid.

TABLE I
ESTIMATED SYSTEM PERFORMANCE BOTH FOR THE PARIS IOD SCENARIO (LEFT COLUMN) AND FOR AN OPERATIONAL SCENARIO (RIGHT COLUMN) [35]

Parameter	IOD	Operational
	Height Accuracy on 100 km, G=23 dBi, h=800 km	Height Accuracy on 100 km, G=30 dBi, h=1500 km
Instrument Noise and Speckle	12.5 cm	4.2 cm
Ionosphere	9.7 cm (2 frequencies)	4.8 cm (3 frequencies)
Troposphere (Wet and Dry)	5 cm	2 cm
Electromagnetic Bias	2 cm	2 cm
Skewness Bias	2 cm	2 cm
Orbit	5 cm	2 cm
Total RMS Height Accuracy	17.5 cm (13 cm at nadir)	7.5 cm (5 cm at nadir)

B. Error Analysis of GNSS-R Interferometric Altimetry

Martin-Neira et al. [35] conducted a comprehensive analysis and description of the mission objectives, performance parameters, system and instrument design, data processing, and accuracy considerations for both the PARIS IOD and the operational interferometric altimetry scenarios. The spaceborne interferometric altimetry scenarios, IOD and operational, were analyzed with an along-track resolution of 100 km and an across-track resolution of 10 km according to Martin-Neira's analysis. In the IOD scenario, with an antenna gain of 23 dBi and an orbit altitude of 800 km, the instrument's ranging accuracy can reach 12.5 cm. After considering the accuracy of dual-frequency ionospheric corrections, as well as corrections for tropospheric, electromagnetic, skewness, and orbit bias, the final accuracy of GNSS-R altimetry can reach 17.5 cm at the edge of the swath. Similarly, in the operational scenario, with an antenna gain of 30 dBi and an orbit altitude of 1500 km, the instrument's ranging accuracy can reach 4.2 cm, resulting in a final GNSS-R altimetry accuracy of 7.5 cm at the edge of the swath. The parameters and accuracies are shown in Table I.

In addition, it should be noted that the accuracy indices in Table I were calculated specifically for the GPS signal by

Matin-Neira. However, previous studies have shown that the altimetry accuracy from the BDS and Galileo signals is superior to that from the GPS signal [41], [42]. Furthermore, different incidence angles have varying effects on the instrument ranging and ionospheric correction accuracy. To simplify the model, we consistently utilized the accuracy results from GPS signal at an incidence angle of 35° during the simulation, even though it results in coarser precision, the error budget remains sufficient.

Satellite altimetry primarily focuses on detecting the short-wavelength components of the marine gravity field. However, Martin-Neira's objective for the PARIS spaceborne scenarios was the detection of ocean currents, and the spatial resolution of PARIS IOD/operational scenarios may not be sufficient for short-wavelength gravity field detection. When the altimetry spatial resolution is too low, the variability at spatial scales is under-represented or not represented, which may result in representativeness errors when inverting the gravity field with high spatial resolution. In fact, the 100-km along-track spatial resolution is achieved through noncoherent integration in order to improve the accuracy of measurements [43]. Therefore, to minimize the impact of representativeness errors, the altimetry resolution of GNSS-R interferometric techniques can be improved by reducing the number of noncoherent integrations. However, as the along-track resolution increases, the noncoherent integration time decreases, leading to a decrease in instrument ranging accuracy and ultimately resulting in a decrease in GNSS-R altimetry precision. The instrument's ranging accuracy σ_{Instu} can be estimated using the following equation:

$$\sigma_{\text{Instu}} = \frac{c}{2 \times \cos\theta} \times \frac{\bar{P}}{\dot{P}} \times \frac{1}{\sqrt{N_{\text{inc}}}} \sqrt{\left(1 + \frac{1}{\text{SNR}}\right)^2 + \left(\frac{1}{\text{SNR}}\right)^2} \quad (1)$$

θ is the angle of signal incidence, \bar{P} is the average power at the specular point, \dot{P} is the derivative of the power waveform also at the specular point, and SNR is the signal-to-noise ratio of the interferometric altimetry. As these parameters have been assumed to be constant, the instrument ranging accuracy σ_{Instu} is only affected by the variation in the number of noncoherent accumulations N_{inc} .

To fulfill the needs of inverting short-wavelength gravity fields, the resolution of GNSS-R interferometric altimetry is set at 10 km in this study. This results in a tenfold decrease in the number of noncoherent accumulations available for integration, leading to a decrease in instrument ranging accuracy to 39.5 cm for PARIS IOD and 13.3 cm for operational. In addition, the lower orbit altitude and faster satellite velocity also contribute to a decrease in noncoherent accumulations for the same along-track resolution. To match the GNSS-R detection capabilities of the FY-3E satellite at an altitude of 836 km, we also considered the impact of orbit altitude changes on instrument ranging accuracy in the PARIS operational scenario. In this case, the instrument ranging accuracy for operational is 14.6 cm, while the orbit altitude for PARIS IOD is almost the same as that of FY-3E, with a negligible impact on accuracy.

In addition, we also considered the effects of the main error correction terms in traditional altimetry methods on the accuracy of GNSS-R altimetry. The final GNSS-R altimetry accuracy can

be calculated using the following equation:

$$\sigma_{\text{ssh}} = \sqrt{\sigma_{\text{Instu}}^2 + \sigma_{\text{Iono}}^2 + \sigma_{\text{Tropo}}^2 + \sigma_{\text{Elect}}^2 + \sigma_{\text{Skewness}}^2 + \sigma_{\text{Orbit}}^2 + \sigma_{\text{Tide}}^2}. \quad (2)$$

The correction accuracy for ionospheric σ_{Iono} , tropospheric σ_{Tropo} , electromagnetic σ_{Elect} , skewness σ_{Skewness} , and orbit corrections σ_{Orbit} can be found in Table I. Despite the potential impact of spatial resolution on tide correction, the difference between GNSS-R interferometric altimetry with a resolution of 10 km and radar altimeters with a resolution of 2 km is minimal. As a result, we set the tide correction accuracy σ_{Tide} to be 3 cm based on the prior experiences with radar altimeters. In addition, considering that the correction errors for geoid and inverted barometer effects are minimal and have almost no impact on the results, we did not take them into account during the simulation process.

Hence, the altimetry accuracy for the IOD and operational scenarios is 41.52 cm and 16.17 cm, respectively, when the along-track resolution is improved to 10 km, taking into consideration the detection capabilities of the FY-3E satellite at its altitude and the instrument detection capabilities of both scenarios. Furthermore, we assume that the system errors can be corrected through calibration and, therefore, did not consider their effect during the simulation.

C. SSH Data Simulation

In order to assess the detection capability of spaceborne GNSS-R interferometric altimetry for the marine vertical deflection and to examine the effects of altimetry error on the accuracy of vertical deflection inversion, two controlled experimental scenarios were conducted: IOD and operational. The IOD and operational scenarios utilized the altimetry capabilities proposed by Martin-Neira in the PARIS IOD and PARIS operational scenarios, respectively. Since the marine gravity field is commonly considered as a steady-state field, the mean sea surface model DTU21MSS with 1' grid was employed as the input for static SSH. Based on the position information of the specular reflection points, the GNSS-R altimetry results for the two controlled experimental scenarios were simulated. The specific steps are shown in Fig. 5.

To capture the impact of spatial smoothing errors in the reflection area of the PAIRS interferometric altimetry on simulated data, the first step is to construct the specular reflection area based on the positions of the FY-3E GNSS-R specular points. Based on the analysis in Section II-A, the resolution of the reflection is set to 10 km in both the across-track and along-track directions. With the selected MSS model possessing a grid resolution of 1 arc-min, which surpasses the spatial resolution of the GNSS-R reflection area, resampling of the constructed GNSS-R specular reflection area becomes necessary. This involves dividing the area into resampled grid points spaced at 2-km intervals along the track and across the track directions (as depicted in Fig. 6).

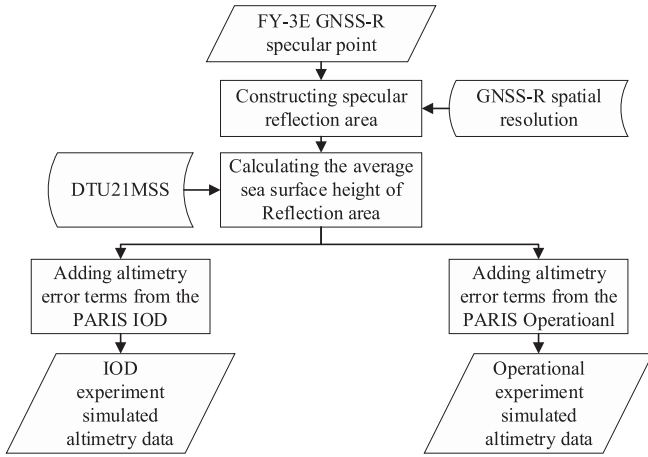


Fig. 5. Flowchart of data simulation process for IOD and operational scenarios.

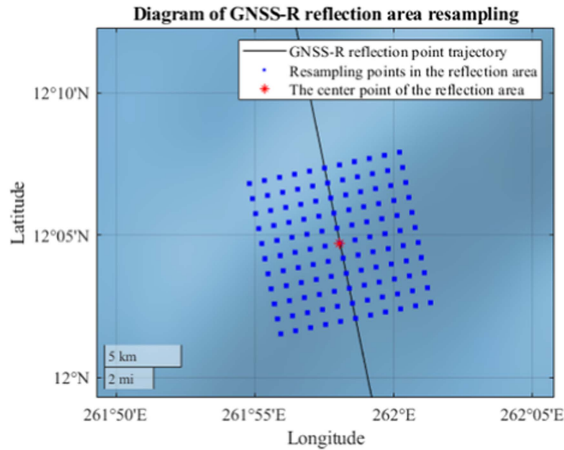


Fig. 6. Diagram of GNSS-R reflection area resampling.

Next, using DTU21MSS as the background field, the SSH values $MSS_{\text{resample_point}}$ for each resampled grid point within the reflection area are interpolated. The SSH at the reflection center point is denoted as $MSS_{\text{sp_point}}$. The average of all $MSS_{\text{resample_point}}$ values within the reflection area provides the SSH $MSS_{\text{reflection}}$ for the GNSS-R specular reflection area.

Finally, the GNSS-R interferometric altimetry error term is introduced by adding a normally distributed error. In practical measurements, there are inherent measurement errors caused by factors, such as instrument limitations and error corrections. Based on the analysis of GNSS-R altimetry accuracy before, the corrected residual error σ_{corr} is assumed to have Gaussian white noise distribution with a mean of 0 and a standard deviation of σ_{ssh} . Then, the simulated corrected residual error is added to the $MSS_{\text{Reflection}}$, resulting in the generation of simulated GNSS-R altimetry results $SSH_{\text{GNSS-R_IOD}}$ and $SSH_{\text{GNSS-R_Ope}}$ for the IOD and operational scenarios, respectively. These simulated GNSS-R altimetry results are then output as the results for the IOD group and the operational scenarios, providing a representation of GNSS-R interferometric altimetry simulation under different scenarios.

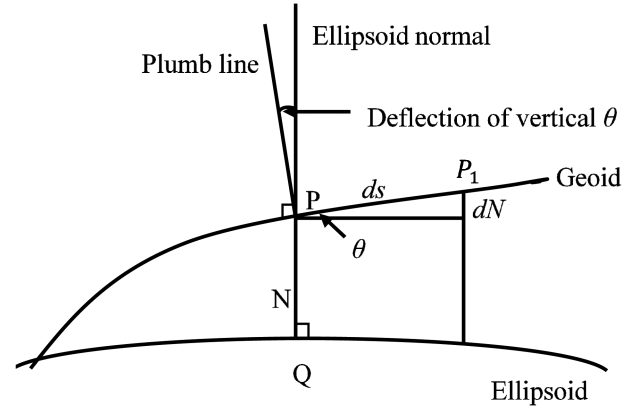


Fig. 7. Schematic of the vertical deflection determination.

D. Inversion and Accuracy Assessment of Vertical Deflection

Vertical deflection refers to the angle between the plumb line and the normal to the ellipsoidal surface at a specific point. As shown in Fig. 7, θ represents the vertical deflection of point P on the geoid surface. Consider a point P_1 at a small distance ds from point P , with a height difference dN between P_1 and P on the geoid surface. According to the definition of vertical deflection, we have the following equation:

$$\theta = -\frac{dN}{ds}. \quad (3)$$

Currently, along-track deflection of vertical (DOV) calculation and crossover point DOV calculation methods are commonly used for inverting vertical deflection from satellite altimetry data [44], [45]. However, they are suitable for local-scale inversion due to their high computational complexity and slow processing speeds. Bao and Lu [46] proposed utilizing a tangent plane of the geoid surface for vertical deflection computation. Based on this, an algorithm using gridded geoid surface heights was developed for rapid inversion, greatly improving efficiency [47]. This study aims to explore the potential of GNSS-R SSH inversion for global-scale vertical deflection and identify factors affecting its accuracy. Therefore, we employ the method based on gridded geoid surface heights for efficient computation of global-scale vertical deflection. The MDT_CNES_CLS18_global model is used to subtract the simulated GNSS-R SSH data from the corresponding ocean mean dynamic topography (MDT) at each measurement point, resulting in the calculation of the geoid surface height (N) for each GNSS-R measurement

$$N = \text{SSH} - \text{MDT}. \quad (4)$$

The geoid surface heights from all measurement points are used to generate a simulated gridded geoid surface through grid processing. Subsequently, the vertical deflection at each grid point is calculated directly from this gridded geoid surface, employing a differencing approach to represent the differences between adjacent discrete grid points. The vertical deflection at the (i,j) grid point can be expressed as the components $\xi(i,j)$ in the

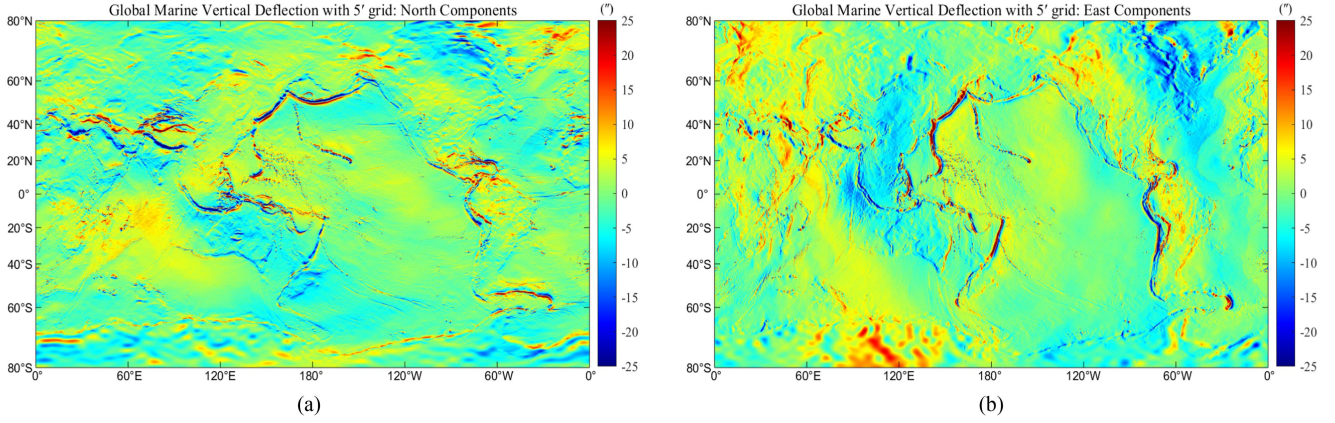


Fig. 8. Global distribution of vertical deflection based on EGM2008 for (a) north–south component and (b) east–west component.

north–south components and $\eta(i, j)$ in the east–west components

$$\xi(i, j) = -\frac{1}{R} \frac{(N_{i+1} - N_i)}{(\varphi_{i+1} - \varphi_i)} \quad (5)$$

$$\eta(i, j) = -\frac{1}{R \cos \varphi_i} \frac{(N_{j+1} - N_j)}{(\lambda_{j+1} - \lambda_j)}. \quad (6)$$

R is the average radius of the Earth, ∂N represents the height difference on the geoid surface, φ represents the latitude, and λ represents the longitude.

In this study, the vertical deflection results from the simulated data are compared with the reference values of the north–south and east–west components, derived from the EGM2008 model. The total accuracy of vertical deflection, denoted as σ_t , was calculated using the following equation:

$$\sigma_t = \sqrt{(\sigma_\xi^2 + \sigma_\eta^2)}. \quad (7)$$

σ_ξ and σ_η represent the accuracy of the north–south and east–west components of vertical deflection, as measured by the standard deviation of their differences from the EGM2008.

The EGM2008 model, released by the National Geospatial-Intelligence Agency, is based on a combined gravity model utilizing GRACE and GEOS data. It offers a high spatial resolution of $2.5' \times 2.5'$ and is widely recognized as one of the most commonly employed geoid models in current practice [48]. Fig. 8 shows the global distribution of vertical deflection for the north–south and east–west components based on EGM2008.

III. RESULTS AND ANALYSIS

A. Simulation Results of Vertical Deflection Based on GNSS-R

To assess the contribution of the spaceborne GNSS-R interferometric altimetry technology to the inversion of vertical deflection, we inverted the results of east–west and north–south components of global $2.5'$, $5'$, and $20'$ grid marine vertical deflection for the IOD and operational scenarios. Simulated data from July 2021 to December 2030 were utilized for the analysis.

Fig. 9 shows the vertical deflection inversion results using the PARIS operational scenario simulation data. The top, middle,

and bottom rows represent the global vertical deflection results for a $2.5'$, $5'$, and $20'$ grid, respectively. The left and right columns correspond to the north–south and east–west components of the vertical deflection. It can be observed that the global $2.5'$ grid vertical deflection results obtained from GNSS-R interferometric altimetry technology exhibit noticeable speckle noise when compared with the vertical deflection results of the EGM2008 model, particularly in the east–west direction of the vertical deflection results at high latitudes. However, the $5'$ and $20'$ grid vertical deflection results do not display such phenomena and retain most of the vertical deflection variation information.

Furthermore, to assess the accuracy of GNSS-R altimetry for different vertical deflection resolutions, we compared the results of vertical deflection from three GNSS-R scenarios with the corresponding vertical deflection from the EGM2008 model at each resolution. It is important to note that the vertical deflection of the EGM2008 model was processed to match the respective resolution for the accurate comparison. In addition, grid points that were not covered were excluded when calculating the mean and standard deviation of the comparison data. The accuracy results are shown in Table II.

Table II presents the average value (mean) and root-mean-square error (RMS) of the residual vertical deflection obtained from the simulation results after subtracting the vertical deflection of the EGM2008 model. According to the results in Table II, in all scenarios, the mean values of the residual vertical deflection are close to 0, providing evidence for the correctness of the data simulation and vertical deflection inversion method. This is because the altimetry error was set as a normally distributed random number with a mean of 0 and a standard deviation of σ_{ssh} in the simulation. In addition, it is expected that the accuracy of the east component vertical deflection is lower than that of the north component in the same scenario due to limitations inherent in the inversion method and the orbit inclination.

According to Table II, the accuracy of GNSS-R interferometric altimetry for global $2.5'$ vertical deflection inversion is $13.772''$ and $5.479''$ for the IOD and operational scenarios, respectively. This indicates that for a $2.5'$ grid resolution of vertical deflection inversion, the altimetry accuracy of spaceborne GNSS-R interferometry has a significant impact on the

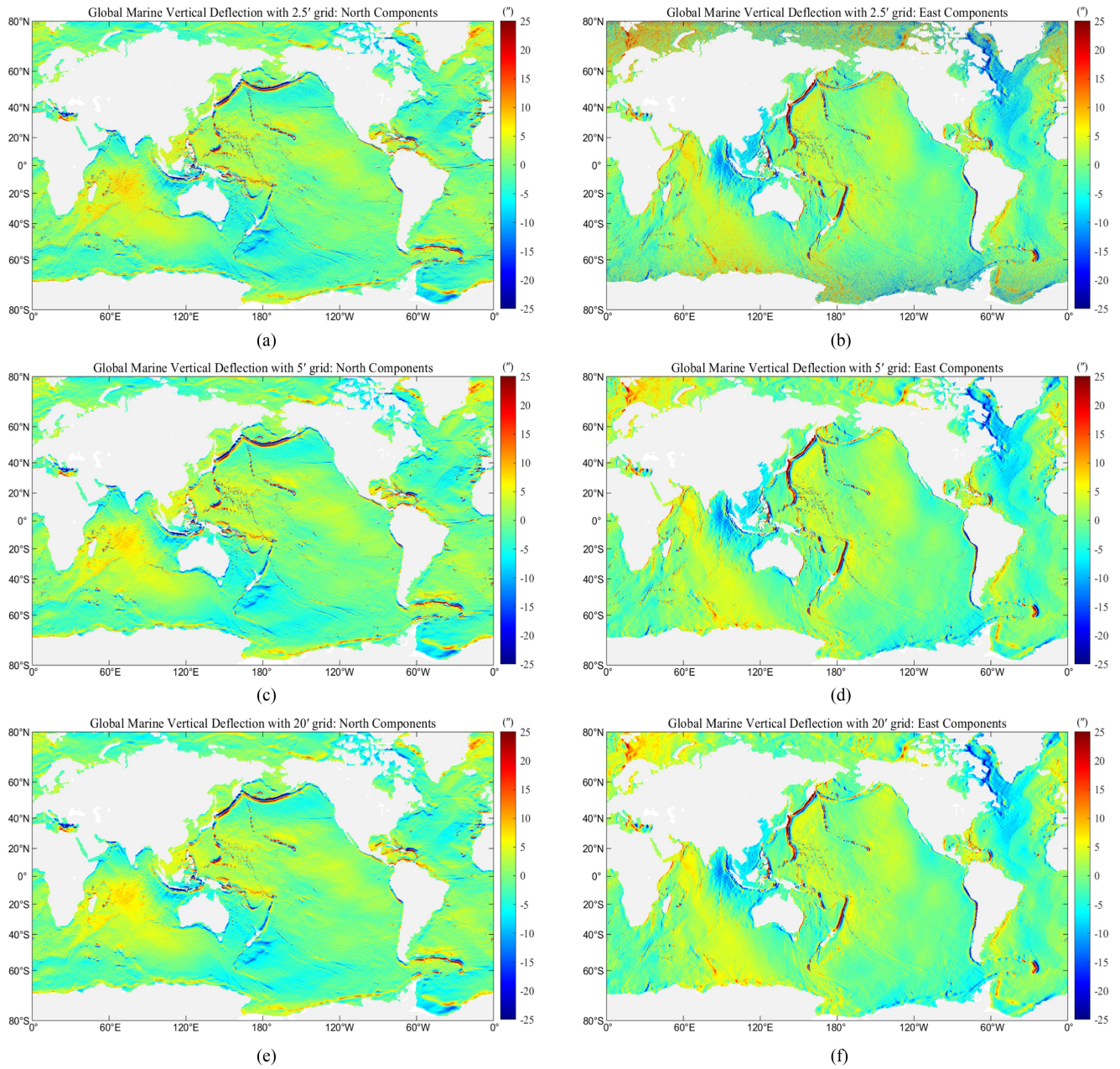


Fig. 9. Global marine vertical deflection simulation results in the PARIS IOD scenario, where (a), (c), and (e) represent the north–south components and (b), (d), and (f) represent the east–west components. Among them, (a) and (b) are the results from a 2.5' grid, (c) and (d) are the results from a 5' grid, and (e) and (f) are the results from a 20' grid.

TABLE II
ACCURACY STATISTICS OF GLOBAL VERTICAL DEFLECTION WITH A 2.5' GRID IN DIFFERENT GNSS-R OBSERVATION SCENARIOS,
COMPARED WITH EGM2008 MODEL

DOV resolution	Scenarios	North component		East component		Total RMS(")
		Mean(")	RMS(")	Mean(")	RMS(")	
2.5'×2.5'	IOD	-0.00002	6.668	-0.00009	12.050	13.772
	Operational	0.00004	2.671	0.00004	4.785	5.479
5'×5'	IOD	0.00003	1.673	-0.00018	3.012	3.445
	Operational	0.000002	0.686	-0.00001	1.205	1.386
20'×20'	IOD	-0.00001	0.111	0.00003	0.194	0.224
	Operational	-0.00002	0.057	-0.00001	0.089	0.106

precision of vertical deflection. In the future, by improving the altimetry accuracy of GNSS-R interferometry, it may be possible to achieve high-precision 2.5' vertical deflection and gravity field results.

For a 5' vertical deflection grid resolution, the accuracies of the IOD and operational scenarios are 3.445'' and 1.386'', respectively. In the operational scenario, both the north–south and east–west components of the vertical deflection exhibited high accuracy, reaching 0.686'' and 1.205'', respectively. In a previous study by Wang et al. [49], SSH measurements from multiple radar altimetry satellites spanning over a decade were used to invert the global 5' × 5' marine vertical deflection. The evaluation showed a precision of 1.12'' for the north–south component and 1.97'' for the east–west component [46]. Comparing these results with the simulated vertical deflection results in the operational scenario, it demonstrates the significant capability of spaceborne GNSS-R interferometric altimetry in vertical deflection and gravity field inversion at a 5' × 5' resolution.

As the grid resolution decreases, the impact of vertical deflection accuracy on the altimetry precision of IOD/operational scenarios decreases as well. At a 20' grid resolution, the overall vertical deflection inversion accuracy in the IOD and operational scenarios reached 0.224'' and 0.106'', respectively. Both the PARIS IOD and operational scenarios achieved high-precision results for global 20' grid vertical deflection. This may be attributed to the lower spatial resolution of spaceborne GNSS-R altimetry, which enhances the representativeness of the altimetry results in the inversion of low-resolution vertical deflection and gravity fields.

B. Effect of GNSS-R Revisit Times

Compared with radar altimeters, the accuracy of spaceborne GNSS-R interferometric altimetry is relatively low. However, it compensates for this with the advantages of rapid global coverage and frequent revisits. Therefore, by utilizing multiple revisits, spaceborne GNSS-R interferometric altimetry has the potential to improve the measurement accuracy of the geoid. The precision of the geoid measurement σ_N after multiple revisits can be determined using (8), which relates it to the accuracy of spaceborne GNSS-R interferometric altimetry σ_h and the average number of global revisits (n)

$$\sigma_N = \frac{\sigma_h}{\sqrt{n}}. \quad (8)$$

Based on (5), (6), and (8), we can utilize the error propagation law to derive the relationship between the accuracy of either the north–south or east–west components of the grid vertical deflection and the measurement accuracy of the geoid height. This relationship is represented by (9) and (10)

$$\sigma_\xi = \frac{\sqrt{2}\sigma_N}{R \cdot \Delta\varphi} \quad (9)$$

$$\sigma_\eta = \frac{\sum_{i=1}^m \sigma_{\eta-\varphi}(i)}{m} = \frac{\sum_{i=1}^m \frac{\sqrt{2}\sigma_N}{R \cdot \Delta\lambda \cdot \cos \varphi_i}}{m}. \quad (10)$$

σ_ξ and σ_η represent the average precision of the north–south and east–west components of the global grid vertical deflection,

respectively. R represents the average radius of the Earth, φ and λ denote the latitude and longitude of the grid points, respectively. $\sigma_{\eta-\varphi}$ represents the precision of the east–west component of the grid vertical deflection at the same latitude. As $\sigma_{\eta-\varphi}$ is associated with latitude φ_i , to calculate the average accuracy of east–west vertical deflection globally, we need to take the average at different latitudes. m represents the number of rows in the grid latitude, and $\Delta\varphi$ and $\Delta\lambda$ are equal to the grid resolution.

Considering the varying proportion of ocean at different latitudes, the accuracy of the east–west component of the vertical deflection σ_η can be further improved, as shown in the following equations:

$$\sigma_\eta = \frac{\sum_{i=1}^n \frac{\sqrt{2}\sigma_N}{R \cdot \Delta\lambda \cdot \cos \varphi_i} \cdot r_i}{\sum_{i=1}^n r_i} \quad (11)$$

$$r_i = \frac{n_{\text{sea}}(i)}{n_{\text{sea}}(i) + n_{\text{land}}(i)}. \quad (12)$$

n_{sea} and n_{land} represent the number of grid points for ocean and land, respectively, at a certain latitude. r_i represents the proportion of ocean grid points at that latitude.

The theoretical accuracy of the vertical deflection's north–south and east–west components can be calculated using (8), (9), (11), and (12) for both IOD and operational altimetry precision scenarios, as shown by the dashed lines in Fig. 10. It should be noted that, in the simulation, we have already processed the observations to ensure that they are independent of each other. The solid lines in the same figure demonstrate the variations in the accuracy of the vertical deflection inversion obtained from simulated IOD and operational altimetry with average global revisit times. The close alignment between the simulation and theoretical accuracy confirms the effectiveness of the simulation and inversion methods. Furthermore, due to the extensive and intricate data processing required in simulation calculations, the theoretical accuracy can be utilized to forecast future variations in vertical deflection accuracy. Initially, as the number of revisit times increases, the accuracy of the vertical deflection inversion experiences rapid improvement. However, as revisit times continue to increase, the rate of improvement diminishes, and the significance of altimetry precision in determining the inversion accuracy becomes more prominent.

The black dashed line in the figures represents the boundary line where the accuracy of vertical deflection is 1''. According to the prediction, it is possible to achieve a vertical deflection product of 2.5' × 2.5' with an accuracy of less than 1'' through an average of 438 global revisits in the operational scenario. With future improvements in GNSS-R interferometric altimetry accuracy or multisatellite network observation, it is possible to achieve a high-precision 2.5' grid vertical deflection. Meanwhile, in an operational scenario, achieving an accuracy of less than 1'' for a global 5' × 5' ocean vertical deflection product would require approximately 108 revisits, which would need a ten-year observation under the detection capability of the L2 data from a single FY-3E satellite.

Importantly, simulation results indicate that the inversion accuracy for a global 20' grid of vertical deflection in GNSS-R interferometric altimetry mode can rapidly reach the 1'' accuracy

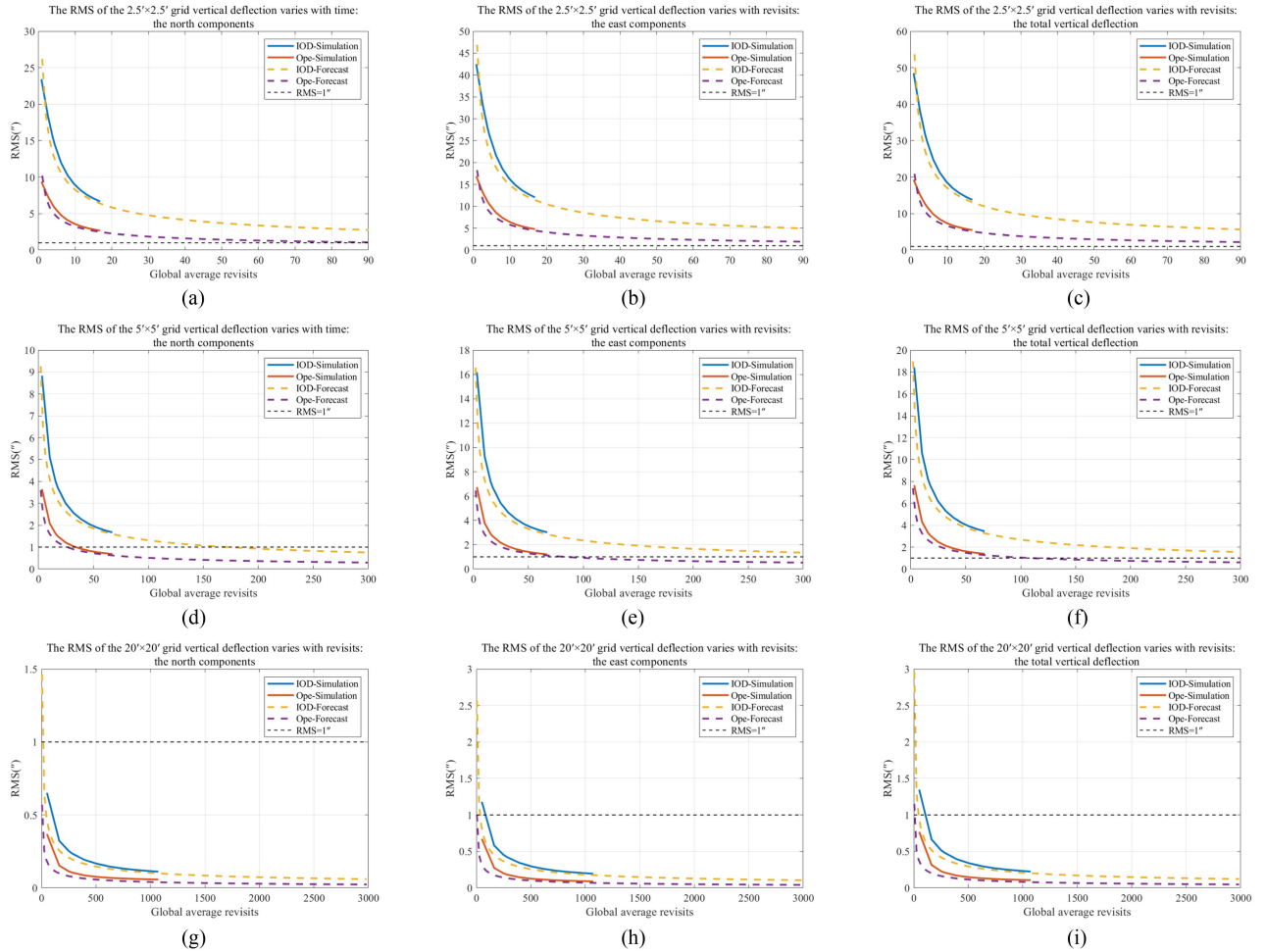


Fig. 10. Vertical deflection precision variations for different GNSS-R long-track resolutions, with (a), (d), and (g) representing the north–south components, (b), (e), and (h) representing the east–west components, and (c), (f), and (i) representing the total vertical deflection precision variations. Among them, (a), (b), and (c) are the results from a $2.5'$ grid, (d), (e), and (f) are the results from a $5'$ grid, and (g), (h), and (i) are the results from a $20'$ grid.

standard, requiring an average of seven global revisit times in the operational scenario. According to the analysis in Section II-B, in the detection scenario using FY-3E L2 data, an average revisit time of over 7.3 times for the entire globe can be achieved within 23 days, covering over 90% of the global ocean regions. Therefore, by leveraging the rapid global coverage capability of GNSS-R technology, there is significant potential to rapidly obtain high-precision global $20'$ vertical deflection and gravity field products, providing stable data for a time-variable gravity field of the global ocean with a $20'$ grid. This optimization would compensate for the higher resolution of time-variable gravity field data provided by satellite gravimetry.

IV. CONCLUSION

The spaceborne GNSS-R interferometric altimetry technology offers advantages, such as low cost, rapid global coverage, and revisiting capability, making it potentially complementary to traditional radar altimeters. This article presents the first simulation study on the measurement capability and potential applications of spaceborne GNSS-R interferometric altimetry technology for global marine vertical deflection inversion.

We employed the configurations of the PARIS IOD and operational scenarios proposed by Martin-Neira as the performance benchmark for spaceborne GNSS-R interferometric altimetry. To meet the demands of high-resolution gravity field detection, we set the along-track resolution of spaceborne GNSS-R interferometric altimetry at 10 km, resulting in the altimetry accuracies of 41.52 cm and 16.17 cm for the IOD and operational scenarios, respectively. In addition, the L2 GNSS-R trajectory data from the FY-3E satellite are utilized to provide the detection capability of spaceborne GNSS-R technology, which has been proven to cover 90% of the global sea area in $20'$ grid within 23 days and 99% within 62 days. Based on this, simulations were conducted on the future trajectory of the GNSS-R payload on FY-3E and the altimetry results of the spaceborne GNSS-R interferometric altimetry. Finally, the accuracy of global marine vertical deflection was evaluated using the simulation results, and a comparison and prediction were made based on the derived theoretical accuracy.

Our results confirm the potential and application value of using spaceborne GNSS-R interferometric altimetry technology for inverting the global marine vertical deflection at $5'$ and $20'$ grid resolutions. In operational altimetry scenario, the

total accuracy of the inverted global ocean vertical deflection using GNSS-R interferometric altimetry simulation is 1.386" and 0.106" for the 5' and 20' grids, respectively. If we consider 1" as the benchmark for accuracy evaluation, the total accuracy of global ocean vertical deflection inversion using the operational altimetry scenario can meet the 1" standard when the global average revisit times of GNSS-R reach approximately 108 and 7 for the 5' and 20' grids, respectively. As the GNSS-R detection on the FY-3E satellite covers 90% of the global sea area in 20' grids within 23 days, with an average revisit time of 7.3, spaceborne GNSS-R interferometric altimetry has the potential to invert the high-precision time-variable gravity field with a 20' resolution, thus compensating for the higher resolution provided by gravity satellites.

For the global 2.5' marine vertical deflection, the accuracy of the north–south and east–west components was 2.671" and 4.785" in the operational scenario, and 6.668" and 12.050" in the IOD scenario, respectively. However, through comparison of the results from the two scenarios, it was found that altimetry accuracy significantly affects the inversion results. Therefore, future improvements in altimetry accuracy and inversion algorithm are essential for enhancing the accuracy of inversion for 2.5' and higher resolution global ocean vertical deflection.

Finally, it should be noted that this study only utilizes L2 GNSS-R trajectory data from the FY-3E single-mission satellite, with an average of 3.2 occupied channels after extensive data screening. Given the advantages of low cost and easy networking of GNSS-R payloads, future efforts can be made to further enhance the application value of spaceborne GNSS-R interferometric altimetry by using multiantenna and multichannel constellation observations.

REFERENCES

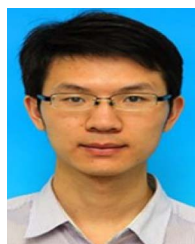
- [1] F. Flechtner, C. Reigber, R. Rummel, and G. Balmino, "Satellite gravimetry: A review of its realization," *Surv. Geophys.*, vol. 42, no. 5, pp. 1029–1074, Sep. 2021, doi: [10.1007/s10712-021-09658-0](https://doi.org/10.1007/s10712-021-09658-0).
- [2] R. F. Annan, X. Wan, R. Hao, and F. Wang, "Global marine gravity gradient tensor inverted from altimetry-derived deflection of the vertical: CUGB2023GRAD," *Earth Syst. Sci. Data*, vol. 16, pp. 1167–1176, 2024, doi: [10.5194/essd-2023-85](https://doi.org/10.5194/essd-2023-85).
- [3] B. F. Chao, "Geodesy is not just for static measurements any more," *Eos Trans. Amer. Geophys. Union*, vol. 84, no. 16, pp. 145–150, Apr. 2003, doi: [10.1029/2003EO160001](https://doi.org/10.1029/2003EO160001).
- [4] T. Zhao et al., "Artificial intelligence for geoscience: Progress, challenges, and perspectives," *Innovation*, vol. 5, no. 5, Sep. 2024, Art. no. 100691, doi: [10.1016/j.xinn.2024.100691](https://doi.org/10.1016/j.xinn.2024.100691).
- [5] M. Abele, J. Balodis, I. Janpaule, I. Lasmane, A. Rubans, and A. Zariņš, "Digital zenith camera for vertical deflection determination," *Geodesy Cartogr.*, vol. 38, no. 4, pp. 123–129, Dec. 2012, doi: [10.3846/20296991.2012.755324](https://doi.org/10.3846/20296991.2012.755324).
- [6] R. P. Middlemiss, A. Samarelli, D. J. Paul, J. Hough, S. Rowan, and G. D. Hammond, "Measurement of the Earth tides with a MEMS gravimeter," *Nature*, vol. 531, no. 7596, pp. 614–617, Mar. 2016, doi: [10.1038/nature17397](https://doi.org/10.1038/nature17397).
- [7] J. Chen et al., "Applications and challenges of GRACE and GRACE follow-on satellite gravimetry," *Surv. Geophys.*, vol. 43, no. 1, pp. 305–345, Feb. 2022, doi: [10.1007/s10712-021-09685-x](https://doi.org/10.1007/s10712-021-09685-x).
- [8] R. McGirr, P. Tregoning, S. Allgeyer, H. McQueen, and A. P. Purcell, "Interplay of altitude, ground track coverage, noise, and regularization in the spatial resolution of GRACE gravity field models," *J. Geophys. Res.*, vol. 128, no. 1, Jan. 2023, Art. no. e2022JB024330, doi: [10.1029/2022JB024330](https://doi.org/10.1029/2022JB024330).
- [9] T. Jin et al., "Analysis of vertical deflections determined from one cycle of simulated SWOT wide-swath altimeter data," *J. Geodesy*, vol. 96, no. 4, Apr. 2022, Art. no. 30, doi: [10.1007/s00190-022-01619-8](https://doi.org/10.1007/s00190-022-01619-8).
- [10] D. Che, H. Li, S. Zhang, and B. Ma, "Calculation of deflection of vertical and gravity anomalies over the South China Sea derived from ICESat-2 data," *Front. Earth Sci.*, vol. 9, May 2021, Art. no. 670256, doi: [10.3389/feart.2021.670256](https://doi.org/10.3389/feart.2021.670256).
- [11] J. Y. Guo, Y. Shen, K. Zhang, X. Liu, Q. Kong, and F. Xie, "Temporal-spatial distribution of oceanic vertical deflections determined by TOPEX/Poseidon and Jason-1/2 missions," *Earth Sci. Res. J.*, vol. 20, no. 2, pp. H1–H5, Jul. 2016, doi: [10.15446/esrj.v20n2.54402](https://doi.org/10.15446/esrj.v20n2.54402).
- [12] O. B. Andersen and P. Knudsen, "The DTU17 global marine gravity field: First validation results," in *Fiducial Reference Measurements for Altimetry*, vol. 150, S. P. Mertikas and R. Pail, Eds. Cham, Switzerland: Springer, 2019, pp. 83–87, doi: [10.1007/1345_2019_65](https://doi.org/10.1007/1345_2019_65).
- [13] D. Sandwell, E. Garcia, K. Soofi, P. Wessel, M. Chandler, and W. H. F. Smith, "Toward 1-mGal accuracy in global marine gravity from CryoSat-2, Envisat, and Jason-1," *Leading Edge*, vol. 32, no. 8, pp. 892–899, Aug. 2013, doi: [10.1190/le32080892.1](https://doi.org/10.1190/le32080892.1).
- [14] C. Hwang, H.-Y. Hsu, and R.-J. Jang, "Global mean sea surface and marine gravity anomaly from multi-satellite altimetry: Applications of deflection-geoid and inverse Vening Meinesz formulae," *J. Geodesy*, vol. 76, no. 8, pp. 407–418, Nov. 2002, doi: [10.1007/s00190-002-0265-6](https://doi.org/10.1007/s00190-002-0265-6).
- [15] J. Richard, V. Enjolras, L. Rys, J. Vallon, I. Nann, and P. Escudier, "Space altimetry from nano-satellites: Payload feasibility, missions and system performances," in *Proc. IEEE Int. Geosci. Remote Sens. Symp.*, Boston, MA, USA, 2008, pp. III–71–III–74, doi: [10.1109/IGARSS.2008.4779285](https://doi.org/10.1109/IGARSS.2008.4779285).
- [16] V. Lopatin and V. Fateev, "Methods of bistatic GNSS-radio altimetry for determining height profile of the ocean and their experimental verification," in *Proc. 5th Symp. Terr. Gravimetry, Static Mobile Meas.*, 2022, pp. 127–132, doi: [10.1007/1345_2022_139](https://doi.org/10.1007/1345_2022_139).
- [17] C. S. Ruf et al., "A new paradigm in Earth environmental monitoring with the CYGNSS small satellite constellation," *Sci. Rep.*, vol. 8, no. 1, Jun. 2018, Art. no. 8782, doi: [10.1038/s41598-018-27127-4](https://doi.org/10.1038/s41598-018-27127-4).
- [18] F. Huang et al., "Assessment of FY-3E GNOS-II GNSS-R global wind product," *IEEE J. Sel. Topics Appl. Earth Observ. Remote Sens.*, vol. 15, pp. 7899–7912, Sep. 2022, doi: [10.1109/JSTARS.2022.3205331](https://doi.org/10.1109/JSTARS.2022.3205331).
- [19] N. Rodriguez-Alvarez, B. Holt, S. Jaruwatanadilok, E. Podest, and K. C. Cavanaugh, "An Arctic sea ice multi-step classification based on GNSS-R data from the TDS-1 mission," *Remote Sens. Environ.*, vol. 230, Sep. 2019, Art. no. 111202, doi: [10.1016/j.rse.2019.05.021](https://doi.org/10.1016/j.rse.2019.05.021).
- [20] C. Yin et al., "Sea ice detection with FY3E GNOS II GNSS reflectometry," in *Proc. IEEE Specialist Meeting Reflectometry Using GNSS Other Signals Opportunity*, Beijing, China, 2021, pp. 36–38, doi: [10.1109/GNSSR53802.2021.9617724](https://doi.org/10.1109/GNSSR53802.2021.9617724).
- [21] C. Yin et al., "Soil moisture retrieval from multi-GNSS reflectometry on FY-3E GNOS-II by land cover classification," *Remote Sens.*, vol. 15, no. 4, Feb. 2023, Art. no. 1097, doi: [10.3390/rs15041097](https://doi.org/10.3390/rs15041097).
- [22] M. Martin-Neira, "A passive reflectometry and interferometry system (PARIS): Application to ocean altimetry," *ESA J.*, vol. 17, no. 4, pp. 331–355, 1993.
- [23] N. Rodriguez-Alvarez, J. F. Munoz-Martin, and M. Morris, "Latest advances in the global navigation satellite system—Reflectometry (GNSS-R) field," *Remote Sens.*, vol. 15, no. 8, Apr. 2023, Art. no. 2157, doi: [10.3390/rs15082157](https://doi.org/10.3390/rs15082157).
- [24] W. Bai et al., "GNSS-R open-loop difference phase altimetry: Results from a bridge experiment," *Adv. Space Res.*, vol. 50, no. 8, pp. 1150–1157, 2012, doi: [10.1016/j.asr.2011.10.019](https://doi.org/10.1016/j.asr.2011.10.019).
- [25] W. Wan et al., "Overview and outlook of GNSS remote sensing technology and applications," *J. Remote Sens.*, vol. 20, no. 5, pp. 858–874, 2016, doi: [10.11834/jrs.20166228](https://doi.org/10.11834/jrs.20166228).
- [26] N. Wang, K. He, F. Gao, T. Chu, J. Hou, and T. Xu, "Analysis of GNSS-R code-level altimetry using QZSS C/A, L1C, and BDS B1C signals and their combinations in a coastal experiment," *IEEE J. Sel. Topics Appl. Earth Observ. Remote Sens.*, vol. 16, pp. 4549–4564, May 2023, doi: [10.1109/JSTARS.2023.3274570](https://doi.org/10.1109/JSTARS.2023.3274570).
- [27] M. Martin-Neira, M. Caparrini, J. Font-Rossello, S. Lannelongue, and C. S. Vallmitjana, "The PARIS concept: An experimental demonstration of sea surface altimetry using GPS reflected signals," *IEEE Trans. Geosci. Remote Sens.*, vol. 39, no. 1, pp. 142–150, Jan. 2001, doi: [10.1109/36.898676](https://doi.org/10.1109/36.898676).
- [28] S. T. Lowe, C. Zuffada, Y. Chao, P. Kroger, L. E. Young, and J. L. LaBrecque, "5-cm-precision aircraft ocean altimetry using GPS reflections," *Geophys. Res. Lett.*, vol. 29, no. 10, May 2002, Art. no. 089532, doi: [10.1029/2002GL014759](https://doi.org/10.1029/2002GL014759).
- [29] M. P. Clarizia, C. P. Gommenginger, S. T. Gleason, M. A. Srokosz, C. Galdi, and M. Di Bisceglie, "Analysis of GNSS-R delay-Doppler maps from the U.K.-DMC satellite over the ocean," *Geophys. Res. Lett.*, vol. 36, no. 2, Jan. 2009, Art. no. 2008GL036292, doi: [10.1029/2008GL036292](https://doi.org/10.1029/2008GL036292).

- [30] G. Foti et al., "Spaceborne GNSS reflectometry for ocean winds: First results from the U.K. TechDemoSat-1 mission," *Geophys. Res. Lett.*, vol. 42, no. 13, pp. 5435–5441, Jul. 2015, doi: [10.1002/2015GL064204](https://doi.org/10.1002/2015GL064204).
- [31] C. S. Ruf, S. Gleason, and D. S. McKague, "Assessment of CYGNSS wind speed retrieval uncertainty," *IEEE J. Sel. Topics Appl. Earth Observ. Remote Sens.*, vol. 12, no. 1, pp. 87–97, Jan. 2019, doi: [10.1109/JSTARS.2018.2825948](https://doi.org/10.1109/JSTARS.2018.2825948).
- [32] G. Yang et al., "FY3E GNOS II GNSS reflectometry: Mission review and first results," *Remote Sens.*, vol. 14, no. 4, Feb. 2022, Art. no. 988, doi: [10.3390/rs14040988](https://doi.org/10.3390/rs14040988).
- [33] M. P. Clarizia, C. Ruf, P. Cipollini, and C. Zuffada, "First spaceborne observation of sea surface height using GPS-reflectometry," *Geophys. Res. Lett.*, vol. 43, no. 2, pp. 767–774, Jan. 2016, doi: [10.1002/2015GL066624](https://doi.org/10.1002/2015GL066624).
- [34] W. Li, E. Cardellach, F. Fabra, S. Ribo, and A. Rius, "Assessment of spaceborne GNSS-R ocean altimetry performance using CYGNSS mission raw data," *IEEE Trans. Geosci. Remote Sens.*, vol. 58, no. 1, pp. 238–250, Jan. 2020, doi: [10.1109/TGRS.2019.2936108](https://doi.org/10.1109/TGRS.2019.2936108).
- [35] M. Martin-Neira, S. D'Addio, C. Buck, N. Floury, and R. Prieto-Cerdeira, "The PARIS ocean altimeter in-orbit demonstrator," *IEEE Trans. Geosci. Remote Sens.*, vol. 49, no. 6, pp. 2209–2237, Jun. 2011, doi: [10.1109/TGRS.2010.2092431](https://doi.org/10.1109/TGRS.2010.2092431).
- [36] M. Martin-Neira, W. Li, A. Andres-Bevide, and X. Ballesteros-Sels, "'Cookie': A satellite concept for GNSS remote sensing constellations," *IEEE J. Sel. Topics Appl. Earth Observ. Remote Sens.*, vol. 9, no. 10, pp. 4593–4610, Oct. 2016, doi: [10.1109/JSTARS.2016.2585620](https://doi.org/10.1109/JSTARS.2016.2585620).
- [37] J. Xie, L. Bertino, E. Cardellach, M. Semmling, and J. Wickert, "An OSSE evaluation of the GNSS-R altimetry data for the GEROS-ISS mission as a complement to the existing observational networks," *Remote Sens. Environ.*, vol. 209, pp. 152–165, 2018, doi: [10.1016/j.rse.2018.02.053](https://doi.org/10.1016/j.rse.2018.02.053).
- [38] J. Saynisch, M. Semmling, J. Wickert, and M. Thomas, "Potential of space-borne GNSS reflectometry to constrain simulations of the ocean circulation: A case study for the South African current system," *Ocean Dyn.*, vol. 65, no. 11, pp. 1441–1460, Nov. 2015, doi: [10.1007/s10236-015-0886-y](https://doi.org/10.1007/s10236-015-0886-y).
- [39] W. Zheng, Z. Li, and F. Wu, "Research progress in improving the accuracy of underwater inertial/gravity integrated navigation based on the new generation of GNSS-R constellation sea surface altimetry principle," *Sci. Technol. Eng.*, vol. 19, no. 36, pp. 21–36, 2019, doi: [10.3969/j.issn.1671-1815.2019.36.002](https://doi.org/10.3969/j.issn.1671-1815.2019.36.002).
- [40] Z. Sun, B. Guan, Z. Zhai, and M. Ouyang, "Research progress of ocean satellite altimetry and its recovery of global marine gravity field and seafloor topography model," *Acta Geodaetica et Cartographica Sinica*, vol. 51, no. 6, pp. 923–934, Jul. 2022, doi: [10.11947/j.AGCS.2022.20220069](https://doi.org/10.11947/j.AGCS.2022.20220069).
- [41] D. Wang et al., "A new GNSS-R interferometric ocean altimetry using Beidou-3 signal," *Chin. J. Space Sci.*, vol. 42, no. 3, 2022, Art. no. 492, doi: [10.11728/cjss2022.03.210315029](https://doi.org/10.11728/cjss2022.03.210315029).
- [42] D. Pascual, A. Camps, F. Martin, H. Park, A. A. Arroyo, and R. Onrubia, "Precision bounds in GNSS-R ocean altimetry," *IEEE J. Sel. Topics Appl. Earth Observ. Remote Sens.*, vol. 7, no. 5, pp. 1416–1423, May 2014, doi: [10.1109/JSTARS.2014.2303251](https://doi.org/10.1109/JSTARS.2014.2303251).
- [43] Z. Li, C. Zuffada, S. T. Lowe, T. Lee, and V. Zlotnicki, "Analysis of GNSS-R altimetry for mapping ocean mesoscale sea surface heights using high-resolution model simulations," *IEEE J. Sel. Topics Appl. Earth Observ. Remote Sens.*, vol. 9, no. 10, pp. 4631–4642, Oct. 2016, doi: [10.1109/JSTARS.2016.2581699](https://doi.org/10.1109/JSTARS.2016.2581699).
- [44] D. T. Sandwell, "Antarctic marine gravity field from high-density satellite altimetry," *Geophys. J. Int.*, vol. 109, no. 2, pp. 437–448, May 1992, doi: [10.1111/j.1365-246X.1992.tb00106.x](https://doi.org/10.1111/j.1365-246X.1992.tb00106.x).
- [45] C. Hwang, E.-C. Kao, and B. Parsons, "Global derivation of marine gravity anomalies from Seasat, Geosat, ERS-1 and TOPEX/POSEIDON altimeter data," *Geophysical J. Int.*, vol. 134, no. 2, pp. 449–459, Aug. 1998, doi: [10.1111/j.1365-246X.1998.tb07139.x](https://doi.org/10.1111/j.1365-246X.1998.tb07139.x).
- [46] L. Bao and Y. Lu, "Recovering deflections of vertical from a tangent plane of gridded geoidal heights from altimetry," in *Satellite Altimetry for Geodesy, Geophysics and Oceanography*, vol. 126, C. Hwang, C. K. Shum, and J. Li, Eds. Berlin, Germany, Springer, 2003, pp. 53–58, doi: [10.1007/978-3-642-18861-9_6](https://doi.org/10.1007/978-3-642-18861-9_6).
- [47] Z. Liu, X. Meng, J. Wang, and Y. Fang, "Parallelization improvement of vertical deviation method in the calculation of sea gravity field," *Prog. Geophys.*, vol. 37, no. 1, pp. 413–420, Feb. 2022, doi: [10.6038/pg2022FF0214](https://doi.org/10.6038/pg2022FF0214).
- [48] N. K. Pavlis, S. A. Holmes, S. C. Kenyon, and J. K. Factor, "The development and evaluation of the Earth gravitational model 2008 (EGM2008)," *J. Geophysical Res.*, vol. 117, no. B4, Apr. 2012, Art. no. B04406, doi: [10.1029/2011JB008916](https://doi.org/10.1029/2011JB008916).
- [49] H. Wang, Y. Wang, and Y. Lu, "High precision vertical deflection over China marginal sea and global sea derived from multi-satellite altimeter," *Geo-Spatial Inf. Sci.*, vol. 11, no. 4, pp. 289–293, Jan. 2008, doi: [10.1007/s11806-008-0122-8](https://doi.org/10.1007/s11806-008-0122-8).



Lichang Duan received the B.S. degree in geodesy and geomatics engineering from the School of Geodesy and Geomatics, Wuhan University, Wuhan, China, in 2020. He is currently working toward the Ph.D. degree in geophysics with National Space Science Center, University of Chinese Academy of Sciences, Beijing, China.

His research interests include global navigation satellite system reflectometry altimetry and its geophysical application.



Junming Xia received the B.S. degree in physics from the Changsha University of Science and Technology, Changsha, China, in 2009, and the M.S. and Ph.D. degrees in Earth and space exploration technology from the University of Chinese Academy of Sciences, Beijing, China, in 2012 and 2015, respectively.

In 2015, he joined the GNSS Remote Sensing Group as an Assistant Researcher with National Space Science Center, Chinese Academy of Sciences, where he has been an Associate Professor since 2019.

His current research interests include GNSS reflection remote sensing and application, electromagnetic scattering models for sea and bare soil surfaces and their inversion, and electromagnetic wave propagation.



Weihua Bai received the Ph.D. degree in space physics from the University of Chinese Academy of Sciences, Beijing, China, in 2008.

He is currently a Professor with National Space Science Center, Chinese Academy of Sciences. He also serves as the Director or Deputy Director of FY3 series GNOS and GNOS II missions. His current research interests include GNSS radio occultation and GNSS-R remote sensing techniques and their applications.



Zhenhe Zhai received the Ph.D. degree in geodesy and survey engineering from The Information Engineering University, Zhengzhou, China, in 2015.

He is currently an Associate Researcher with the State Key Laboratory of Geo-Information Engineering, Beijing, China. His research interests include spatial geodesy and vertical datum of surveying and mapping.



Feixiong Huang (Member, IEEE) received the B.S. degree in geodesy and geomatics engineering from Wuhan University, Wuhan, China, in 2014, and the Ph.D. degree in aeronautical and astronautical engineering from Purdue University, West Lafayette, IN, USA, in 2020.

He was a Visiting Scientist with Royal Netherlands Meteorological Institute, De Bilt, The Netherlands, in summer 2019 with funding from the EUMETSAT OSI SAF Visiting Scientist Program. He is currently an Associate Professor with National Space Science

Center, Chinese Academy of Sciences, Beijing, China. His research interests include spaceborne GNSS-R, microwave ocean remote sensing, and data assimilation.



Cong Yin received the B.S., M.S., and Ph.D. degrees in atmosphere physics from the Nanjing University of Information Science and Technology, Nanjing, China, in 2008, 2011, and 2019, respectively.

She is currently working with National Space Science Center, Chinese Academy of Sciences, Beijing, China. Her research interests include Earth surface remote sensing with GNSS-R techniques.



Yixuan Sun received the master's degree in electronic and communication engineering from the School of Electronic Information Engineering, Beihang University, Beijing, China, in 2021. She is currently working toward the Ph.D. degree in geophysics with the National Space Science Center, University of Chinese Academy of Sciences, Beijing.

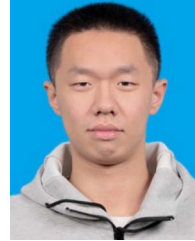
Her research interests include GNSS-R model.



Yueqiang Sun received the B.S. degree in radio physics from Nanjing University, Nanjing, China, in 1985, and the Ph.D. degree in space physics from the University of Chinese Academy of Sciences, Beijing, China, in 2002.

She is currently a Professor with National Space Science Center, Chinese Academy of Sciences, Beijing, China. She devotes to develop GNSS remote sensing and spaceborne spatial environment exploration technologies. She has been the Principal Investigator or Vice Principal Investigator of more than

20 missions/projects in manned space flight, FengYun, and National Natural Science Foundation (863) areas. Her interested research areas include GNSS radio occultation, GNSS-R remote sensing techniques, atmospheric physics, ionospheric physics, magnetic physics, space physics, and so on.



Shengyu Kang received the B.S. degree in computer science and technology in 2021 from the University of Science and Technology, Beijing, China, where he is currently working toward the Ph.D. degree in computer science and technology.

His research interests include parallel computing, GNSS signal processing, and intelligent signal processing.



Qifei Du received the Ph.D. degree in space physics from the University of Chinese Academy of Sciences, Beijing, China, in 2012.

He is currently a Professor with National Space Science Center, Chinese Academy of Sciences. His research field is spaceborne applications of GNSS signal, including GNSS occultation and GNSS-R remote sensing. His interested technical fields are GNSS receiver, antenna, and microwave circuits development. He was the Principal Investigator of the occultation payloads for Yinghuo Satellite and Fengyun-3 Satellites.



Guanyi Wang received the B.S. degree in atmospheric sciences from the Nanjing University of Information Science and Technology (NUIST), Nanjing, China, in 2022. She is currently working toward the Ph.D. degree in geophysics with the National Space Science Center (NSSC), Chinese Academy of Sciences (CAS), Beijing, China.

Her research focuses on the assimilation of spaceborne GNSS remote sensing data for weather research and forecasting model.



Dongwei Wang received the Ph.D. degree in Earth and space probing technology from the University of Chinese Academy of Sciences, Beijing, China, in 2021.

He is currently an Associate Professor with National Space Science Center, Chinese Academy of Sciences. His research fields include GNSS remote sensing technologies and embedded system design and development.



Xiaofeng Meng received the B.S. degree in ecology from Guangxi University, Nanning, China, in 2023. He is currently working toward the M.Sc. degree in Earth and space probing technology with the University of Chinese Academy of Sciences, Beijing, China.

His research interests include GNSS-R remote sensing technologies, GNSS-R land remote sensing, and GNSS-R soil freeze-thaw state retrieval.



Xianyi Wang received the M.S. and Ph.D. degrees in space physics from the University of Chinese Academy of Sciences, Beijing, China, in 2007 and 2012, respectively.

He is currently a Professor with National Space Science Center (NSSC), Chinese Academy of Sciences (CAS). His research interests include GNSS remote sensing technologies and applications, GNSS signal processing, navigation, communication, and embedded system design and development.



Yunlong Du received the B.Eng. degree in remote sensing science and technology from Chang'an University, Xi'an, China, in 2023. He is currently working toward the Ph.D. degree in Earth and space probing with the University of Chinese Academy of Sciences, Beijing, China.

His research interests include GNSS signal processing and GNSS-R remote sensing.